Journal of Science and Transport Technology
Journal homepage: https://jstt.vn/index.php/en

Nonlinear thermo-mechanical buckling responses of FG-GPLRC catenary caps and circular plates

Kieu Quang Thai[1], Bui Tien Tu[2*], Cao Cong Anh[1,3]
[1]Graduate University of Science and Technology, Vietnam Academy of Science and Technology, Hanoi, Vietnam
[2]Mechanics of Advanced Materials and Structures, University of Transport Technology, Hanoi, Vietnam
[3]University of Transport Ho Chi Minh City, Ho Chi Minh City, Vietnam

Article info
Type of article:
Original research paper

DOI:
https://doi.org/10.58845/jstt.utt.2026.en.6.2.98-115

***Corresponding author:**
Email address:
tubt@utt.edu.vn

Received: 09/09/2025
Received in Revised Form: 15/11/2025
Accepted: 18/12/2025

Abstract: An analytical framework is developed to investigate the nonlinear thermal and mechanical buckling behavior of functionally graded graphene platelet-reinforced composite (FG-GPLRC) catenary caps resting on nonlinear elastic foundations. The formulation is based on the first-order shear deformation theory (FSDT) coupled with von Kármán-type geometric nonlinearity. The cap geometry follows a catenary profile, from which spherical caps and circular plates emerge as special cases when the curvature radius is constant or tends to infinity, respectively. The graphene platelets are embedded within a copper matrix and graded through the thickness using various distribution patterns. By employing the Galerkin method, explicit expressions for thermal critical loads and postbuckling paths under both thermal and external pressure are derived. A comprehensive parametric study is performed to examine the influences of cap geometry, foundation parameters, and GPL distribution on the stability characteristics, offering insights into the design of curved FG-GPLRC structures under combined loading conditions.

Keywords: Buckling and Postbuckling, Catenary cap, Functionally graded graphene platelets reinforced composite, Thermal load, External pressure.

1. Introduction

In contemporary engineering applications, circular plates and shell-type caps have gained widespread utilization in fields such as marine engineering, civil infrastructure, and aerospace systems due to their structural simplicity, manufacturing feasibility, and high efficiency in load-bearing performance.

Functionally graded materials (FGMs), characterized by the gradual variation in composition between metallic and ceramic phases, effectively mitigate stress concentrations caused by mismatched material properties. This continuous gradation results in enhanced thermal resistance, mechanical strength, and structural integrity. Consequently, FGMs have been extensively investigated in structural applications subjected to combined thermal and mechanical loading, particularly in circular plates and spherical caps. Numerous studies have explored the stability and vibration behavior of FGM circular plates through analytical, semi-analytical, and numerical methods under various boundary conditions and theoretical frameworks [1–6]. In comparison,

annular plates and shallow spherical caps composed of FGMs present greater modeling challenges due to their more complex geometries. These structures have attracted increasing attention in recent years [6–12]. By introducing the assumption of shallow curvature, researchers have simplified the governing equations by transforming from spherical to polar coordinates. However, this geometric simplification does not reduce the complexity of the thermo-mechanical behavior, which remains significantly richer than that of flat circular plates.

Functionally graded graphene platelet-reinforced composites (FG-GPLRCs) represent a class of advanced materials in which graphene platelets are distributed non-uniformly through the thickness, offering simultaneous improvements in mechanical strength and thermal resistance. The application of first-order shear deformation theory (FSDT) combined with the Galerkin method has enabled the analysis of various nonlinear behaviors in FG-GPLRC structures, such as aero-thermo-elastic flutter and dynamic responses of stiffened porous plates and cylindrical shells [13, 14]. Further studies have addressed porous FG-GPLRC annular sector plates, focusing on their shear buckling characteristics, static responses, natural frequencies, and dynamic behaviors using both three-dimensional elasticity formulations, FSDT, and HSDT [15-17]. Circular plates and spherical caps made of FG-GPLRCs have also been widely studied under diverse boundary and loading conditions, encompassing problems such as nonlinear vibration, dynamic buckling, bending, and thermo-mechanical instability [18–28]. In particular, Nam et al. [29] proposed an enhanced smeared stiffener modeling approach using a one-step spiderweb scheme to analyze the nonlinear buckling behavior of FG-GPLRC spherical and circular plates, demonstrating the stiffeners' significant contribution to structural performance.

In recent years, traditional shell forms such as spherical caps with constant curvature, while structurally efficient, have become less adequate in addressing the evolving demands of modern engineering applications. Increasingly complex architectural forms, aesthetic considerations, and stringent performance requirements necessitate the exploration of more versatile geometries [30–34].

Despite their potential, shell caps with non-uniform curvature, such as those deviating from classical spherical shapes, remain underexplored, particularly in the context of their thermo-mechanical behavior. This gap is largely attributable to the mathematical complexity associated with modeling such geometries, which poses significant analytical and computational challenges.

Unlike conventional spherical or parabolic caps, catenary caps exhibit a non-uniform curvature that offers enhanced geometric flexibility. This allows designers to tailor shell profiles for specific performance or aesthetic criteria, facilitating optimized stress distribution and architectural adaptability. Such versatility makes catenary shells particularly appealing in modern structural and composite design, even though their load-bearing advantages may depend on specific loading scenarios. Despite their promising characteristics, studies on the thermo-mechanical buckling responses of such shells remain limited, especially in the context of advanced FG-GPLRC materials.

This study focuses on a novel FG-GPLRC shell structure, catenary caps, which rest on nonlinear elastic foundations and are subjected to uniformly distributed thermal and external pressure loads. The catenary curvature provides a generalized geometric framework, wherein spherical caps and flat circular plates emerge as limiting cases corresponding to constant or infinite curvature radius, respectively. The governing nonlinear equilibrium equations are formulated using the FSDT, incorporating geometric

nonlinearity of the von Kármán type. An approximate analytical solution is obtained through the Galerkin method, enabling the derivation of critical buckling loads and postbuckling responses. The study further explores the effects of cap geometry, foundation characteristics, and GPL distribution patterns on the thermo-mechanical stability of the structure, offering new insights into the design and performance of functionally graded, curved composite shells.

2. Configurations and FG-GPLRC properties of catenary caps

Fig. 1 illustrates the configuration of an FG-GPLRC catenary cap. The geometrical properties are presented with the radius of cap projection a, cap thickness h, radius of curvature $R(r)$, rise of the cap top Y. Due to the shallow geometric characteristic, the simpler coordinate system (r,θ,z) can be introduced. The caps are resting on the nonlinear elastic foundation with three-parameter model, including linear parameters K_1, K_2, and nonlinear parameter K_3. The catenary caps are assumed to be clamped along their edges, imposing zero displacement and rotation, and considered to be under external pressure q and uniformly distributed thermal load ΔT.

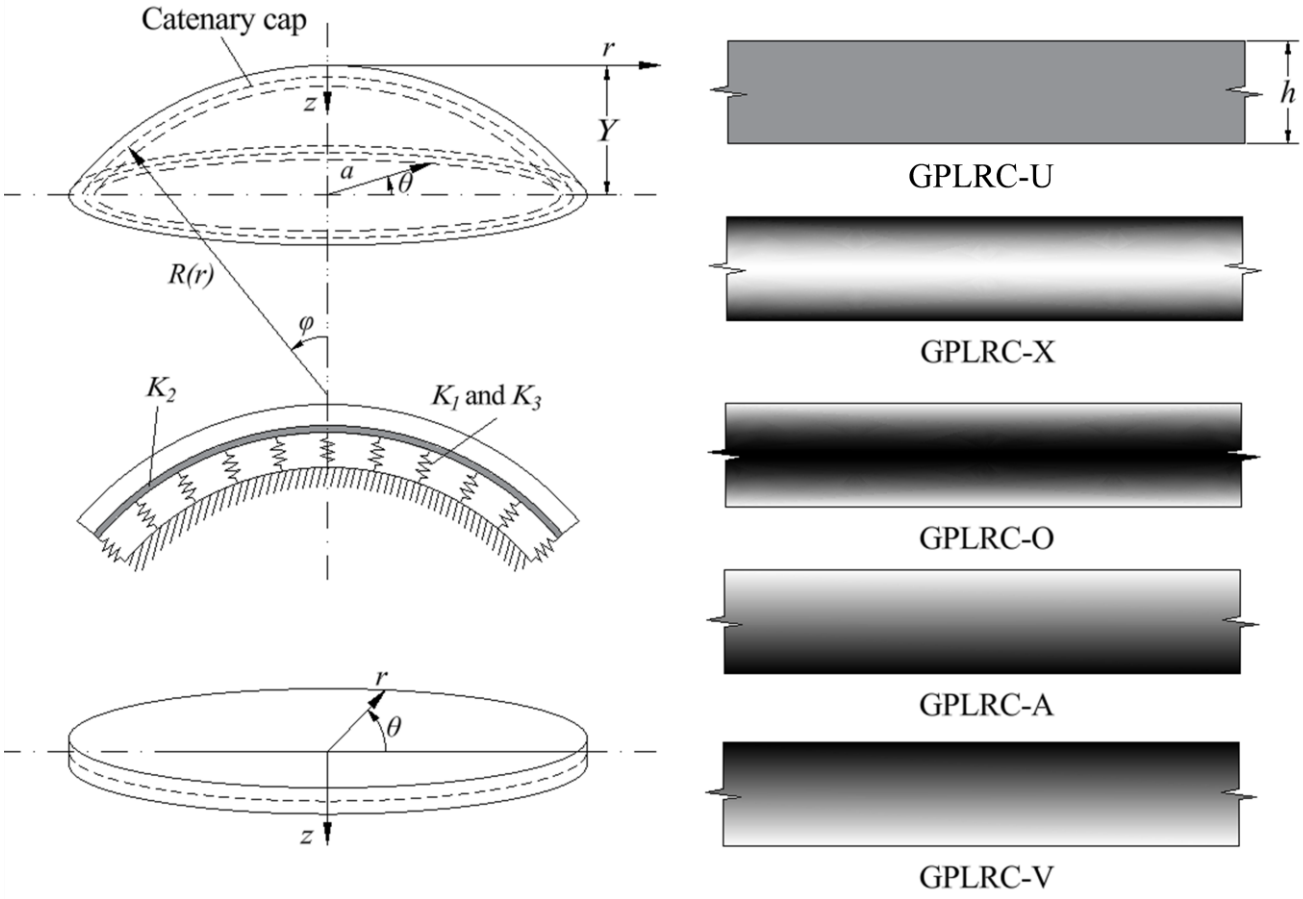

Fig. 1. Configuration of FG-GPLRC catenary caps and coordinate system

The radius of curvature $R(r)$ of catenary caps determined, as

$$y_{catenary} = Y - A\left[\cosh\left(\frac{r}{A}\right) - 1\right],$$

$$a = A\,\text{arc}\cosh\left(1 + \frac{Y}{A}\right),$$

$$R_{(r)catenary} = A\cosh^2\left(\frac{r}{A}\right), \quad (1)$$

where A is the catenary parameters.

Five different GPL distribution laws GPLRC-O, GPLRC-X, GPLRC-U, GPLRC-V, and GPLRC-A are considered.

Based on the extended Halpin-Tsai model, the Young's modulus of the catenary caps is predicted by [29]

$$E(z)=\frac{3E_m}{8}\left[\frac{\Omega_1\tau_1V_{GPL}(z)+1}{-\tau_1V_{GPL}(z)+1}+\frac{5}{3}\frac{\Omega_2\tau_2V_{GPL}(z)+1}{-\tau_2V_{GPL}(z)+1}\right], \quad (2)$$

where

$$\tau_1=\frac{\mu-1}{\mu+\Omega_1},\ \tau_2=\frac{\mu-1}{\mu+\Omega_2},$$

$$\Omega_1=2\left(\frac{i_{GPL}}{z_{GPL}}\right),\ \Omega_2=2\left(\frac{j_{GPL}}{z_{GPL}}\right),\mu=\frac{E_{GPL}}{E_m},$$

with E is the denote of Young's modulus, the subscripts m and GPL are the denotes of matrix and GPL, respectively. i_{GPL}, j_{GPL} and z_{GPL} are the GPL length, width and thickness, respectively, and V_{GPL} is the volume fraction of the GPL $(V_m+V_{GPL}=1)$, defined as

$$V_{GPL}(z)=\frac{\Lambda_{GPL}}{\Lambda_{GPL}+(\rho_{GPL}/\rho_m)(1-\Lambda_{GPL})}, \quad (3)$$

where ρ is the denote of the densities, Λ_{GPL} is the mass fraction of GPL, which depends on five distribution laws of GPL, according to

$$\Lambda_{GPL}(z)=\begin{cases}T_{GPL}+2T_{GPL}\dfrac{z}{h}\ \text{for}\ \dfrac{-h}{2}\le z\le\dfrac{h}{2},\text{GPLRC-A},\\ 4\dfrac{|z|}{h}T_{GPL}\ \text{for}\dfrac{-h}{2}\le z\le\dfrac{h}{2},\text{GPLRC-X},\\ T_{GPL}\ \text{for}\dfrac{-h}{2}\le z\le\dfrac{h}{2},\text{GPLRC-U},\\ 2T_{GPL}-4T_{GPL}\dfrac{|z|}{h}\ \text{for}\ \dfrac{-h}{2}\le z\le\dfrac{h}{2},\text{GPLRC-O},\\ T_{GPL}-2T_{GPL}\dfrac{z}{h}\ \text{for}\ \dfrac{-h}{2}\le z\le\dfrac{h}{2},\text{GPLRC-V},\end{cases} \quad (4)$$

where T_{GPL} is the total GPL mass fraction.

Poisson's ratio and thermal expansion coefficient are estimated according to the rule of mixture, as

$$\nu(z)=\nu_{GPL}V_{GPL}+\nu_m-\nu_mV_{GPL},$$
$$\alpha(z)=\alpha_{GPL}V_{GPL}+\alpha_m-\alpha_mV_{GPL}. \quad (5)$$

3. Fundamental formulations

According to the FSDT, the displacements ($\bar{u}$, $\bar{v}$, $\bar{w}$) at any point on the cap thickness and the mid-plane displacements (u, v, w) are related according to the following expressions [11]

$$\bar{u}(r,z)=u(r)+z\psi(r),$$
$$\bar{v}(r,z)=0, \quad (6)$$
$$\bar{w}(r,z)=w(r)+L(r),$$

where the axisymmetric deformation assumption is considered for the caps, the geometrical imperfection and rotation are denoted by $L(r)$ and $\psi(r)$.

The strains are expressed through the corresponding mid-plane strains ε_r^0, ε_θ^0 and deformation curvatures χ_r, χ_θ, as

$$\begin{Bmatrix}\varepsilon_r\\ \varepsilon_\theta\\ \gamma_{rz}\end{Bmatrix}=\begin{Bmatrix}\varepsilon_r^0+z\chi_r\\ \varepsilon_\theta^0+z\chi_\theta\\ \psi+w_{,r}\end{Bmatrix},$$

$$\begin{Bmatrix}\varepsilon_r^0\\ \varepsilon_\theta^0\end{Bmatrix}=\begin{Bmatrix}u_{,r}+\frac{1}{2}w_{,r}^2+w_{,r}L_{,r}-\frac{w}{R}\\ \frac{u}{r}-\frac{w}{R}\end{Bmatrix}, \quad (7)$$

$$\begin{Bmatrix}\chi_r\\ \chi_\theta\end{Bmatrix}=\begin{Bmatrix}\psi_{,r}\\ \frac{\psi}{r}\end{Bmatrix}.$$

The stress-strain expressions can be applied, considering the thermal stresses ΔT, as

$$\begin{Bmatrix}\sigma_r\\ \sigma_\theta\end{Bmatrix}=\frac{Ez\lambda}{1-[\nu z\lambda]^2}\begin{Bmatrix}1 & \nu z\lambda\\ \nu z\lambda & 1\end{Bmatrix}\begin{Bmatrix}\varepsilon_r\\ \varepsilon_\theta\end{Bmatrix}$$
$$-\frac{Ez\lambda}{1-\nu z\lambda}\alpha z\lambda\begin{Bmatrix}\Delta T\\ \Delta T\end{Bmatrix}, \quad (8)$$
$$\tau_{rz}=\frac{Ez\lambda}{2[1+\nu z\lambda]}\gamma_{rz},$$
$$\lambda=\frac{1}{h}.$$

The internal forces of catenary caps are calculated as

$$\left(N_r, M_r, N_\theta, M_\theta, Q_r\right) = \int_{-h/2}^{h/2} \left(\sigma_r, z\sigma_r, \sigma_\theta, z\sigma_\theta, \tau_{rz}\right) dz. \quad (9)$$

The force and moment resultants are calculated using Eqs. (14-16), presented as

$$\begin{Bmatrix} N_r \\ N_\theta \\ M_r \\ M_\theta \\ Q_r \end{Bmatrix} = -\begin{Bmatrix} \Phi_1 \\ \Phi_1 \\ \Phi_2 \\ \Phi_2 \\ 0 \end{Bmatrix} + \begin{bmatrix} A_{11} & A_{12} & B_{11} & B_{12} & 0 \\ A_{12} & A_{22} & B_{12} & B_{22} & 0 \\ B_{11} & B_{12} & D_{11} & D_{12} & 0 \\ B_{12} & B_{22} & D_{12} & D_{22} & 0 \\ 0 & 0 & 0 & 0 & K_s H_{44} \end{bmatrix} \begin{Bmatrix} \varepsilon_r^0 \\ \varepsilon_\theta^0 \\ \chi_r \\ \chi_\theta \\ \psi + w_{,r} \end{Bmatrix}, \quad (10)$$

where $K_s = 5/6$ is the shear correction factor, Φ_1 and Φ_2 are the thermal force and moment, respectively, and

$$\left(A_{ij}, B_{ij}, D_{ij}, H_{ij}\right) = \int_{-\frac{h}{2}}^{\frac{h}{2}} \left(1, z, z^2, 1\right) Q_{ij} dz,$$

$$\Phi_1 = \Gamma_1 \Delta T, \quad \Gamma_1 = \int_{-\frac{h}{2}}^{\frac{h}{2}} \alpha \left(Q_{12} + Q_{11}\right) dz,$$

$$Q_{11} = \frac{Ez\lambda}{1 - \nu^2 z^2 \lambda^2} = Q_{22},$$

$$Q_{12} = \nu z\lambda \frac{Ez\lambda}{1 - \nu^2 z^2 \lambda^2},$$

$$Q_{44} = \frac{Ez\lambda}{2\nu z\lambda + 2}.$$

According to the FSDT, the equilibrium equations of catenary caps, considering the cap-foundation interaction in the nonlinear foundation model are expressed as

$$\begin{aligned} &\left(rN_r\right)_{,r} - N_\theta = 0, \\ &\left(rM_r\right)_{,r} - M_\theta - Q_r r = 0, \\ &\left(rQ_r\right)_{,r} + \left[N_r\left(w_{,r} + L_{,r}\right)r\right]_{,r} + \left(N_\theta + N_r\right)\frac{r}{R} + \\ &\left[q - K_1 w + K_2\left(w_{,rr} + \frac{1}{r}w_{,r}\right) - K_3 w^3\right] r = 0, \end{aligned} \quad (11)$$

Based on the Eqs. (10) and (7), the equilibrium equations (11) are re-established with respect to u, ψ and w, as

$$\begin{aligned} &\frac{A_{22}w}{R} - \frac{A_{22}u}{r} + \frac{A_{11}w_{,r}^2}{2} - \frac{A_{11}w_{,r}}{R}r - \frac{A_{12}w_{,r}^2}{2} \\ &- \frac{rA_{12}w_{,r}}{R} - \frac{B_{22}\psi}{r} - \frac{A_{11}w}{R} + A_{11}w_{,r}L_{,r} \\ &+ B_{11}\psi_{,r} + A_{11}u_{,r} + B_{11}\psi_{,rr}r + A_{11}w_{,r}L_{,rr}r \\ &- A_{12}w_{,r}L_{,r} + A_{11}u_{,rr}r + rA_{11}w_{,r}w_{,rr} \\ &+ A_{11}w_{,rr}L_{,r}r = 0, \end{aligned} \quad (12)$$

$$\begin{aligned} &\frac{B_{11}w_{,r}^2}{2} - \frac{B_{12}w_{,r}}{R}r - \frac{D_{22}\psi}{r} - \frac{B_{12}w_{,r}^2}{2} \\ &- \frac{B_{11}w_{,r}}{R}r - \frac{B_{11}w}{R} - \frac{B_{22}u}{r} + \frac{B_{22}w}{R} \\ &B_{11}u_{,r} + B_{11}w_{,r}w_{,rr}r + B_{11}u_{,rr}r \\ &+ B_{11}w_{,r}L_{,r} + B_{11}w_{,rr}L_{,r}r + B_{11}w_{,r}L_{,rr}r \\ &+ D_{11}\psi_{,rr}r - B_{12}w_{,r}L_{,r} + D_{11}\psi_{,r} \\ &- K_s H_{44} w_{,r} r - K_s H_{44}\psi r = 0, \end{aligned} \quad (13)$$

$$\begin{aligned} &\left[-\frac{w}{R}\left(L_{,r} + w_{,r}\right)r - \frac{w}{R}\left(L_{,r} + w_{,r}\right)\right. \\ &+ 3L_{,r}w_{,r}\,w_{,rr}\,r + L_{,rr}{}^2 w_{,r} + u_{,rr}\left(w_{,r} + L_{,r}\right)r \\ &+ \frac{wR_{,r}}{R^2}\left(L_{,r} + w_{,r}\right)r + w_{,rr}\,L_{,r}{}^2 r + \frac{1}{2}w_{,r}{}^3 \\ &+ u_{,r}\left(\frac{1}{R} + w_{,rr} + L_{,rr}\right)r - \frac{1}{2}\frac{w_{,r}{}^2}{R}r \\ &+ \frac{3}{2}w_{,r}{}^2\left(w_{,rr} + L_{,rr}\right)r + u_{,r}\left(L_{,r} + w_{,r}\right) \\ &\left. - \frac{w}{R^2}r + 2w_{,r}\,L_{,rr}\,L_{,r}r + \frac{3}{2}w_{,r}{}^2 L_{,r}\right]A_{11} \\ &- \Phi_1\left(w_{,rr} + L_{,rr}\right)r + \left(\frac{u}{R} - \frac{w}{R^2}r\right)A_{22} \\ &- \frac{2}{R}\Phi_1 r + \frac{B_{22}}{R}\psi + \left[\frac{r}{R^2}R_{,r}w\left(L_{,r} + w_{,r}\right)\right. \\ &+ \frac{1}{R}u_{,r}r - \frac{1}{R}\left(L_{,rr} + w_{,rr}\right)wr - \frac{1}{2}\frac{w_{,r}{}^2}{R}r \\ &- \frac{w}{R}\left(w_{,r} + L_{,r}\right) + \frac{u}{R} + u\left(L_{,rr} + w_{,rr}\right) \\ &\left. - \frac{2}{R^2}wr + u_{,r}\left(w_{,r} + L_{,r}\right)\right]A_{12} \\ &- \Phi_1\left(w_{,r} + L_{,r}\right) + \left[\left(w_{,r} + L_{,r}\right)\psi_{,r} + \frac{\psi_{,r}}{R}r\right. \end{aligned}$$

$$+\psi_{,rr}\left(w_{,r}+L_{,r}\right)r+\left(L_{,rr}+w_{,rr}\right)\psi_{,r}\,r\Big]B_{11}$$
$$+\left[\frac{\psi}{R}+\frac{\psi_{,r}}{R}r+\left(L_{,rr}+w_{,rr}\right)\psi\right.$$
$$\left.+\psi_{,r}\left(w_{,r}+L_{,r}\right)\right]B_{12}+K_2\,w_{,r}+qr \qquad (14)$$
$$-K_3\,w^3r-K_1\,wr+K_2\,w_{,rr}r$$
$$+K_sH_{44}\psi(r)+K_sH_{44}\frac{d}{dr}w(r)=0.$$

4. Solution forms and Galerkin method

The axisymmetric assumption at the top (at $r=0$) and the clamped edge contour (at $r=a$) are considered. The corresponding boundary conditions are presented as

$$\begin{aligned} &u=0,\psi=0,w=\text{finite}, \quad \text{At} \quad r=0,\\ &w=0,\ \psi=0,\ u=0, \quad \text{At} \quad r=a. \end{aligned} \qquad (15)$$

To satisfy the conditions (15), the approximate forms of the displacements, rotation, and imperfection are chosen by [35]

$$u=U\sin\left(\frac{m\pi r}{a}\right),\quad \psi=\Psi\sin\left(\frac{m\pi r}{a}\right),$$
$$w=W\left[\cos\left(\frac{m\pi r}{2a}\right)\right]^2,\quad L=L_D\left[\cos\left(\frac{m\pi r}{2a}\right)\right]^2, \qquad (16)$$

where the amplitudes of displacement, deflection, rotation, and imperfection are denoted by U, W, Ψ, and L_D; m is the meridional buckling mode.

Substituting Eq. (16) into Eqs. (12)-(14), and applying the Galerkin method, leads to

$$P_{11}W^2+W\left(P_{12}+P_{13}L_D\right)+P_{14}U+P_{15}\Psi=0, \qquad (17)$$
$$P_{21}W^2+W\left(P_{22}+P_{23}L_D\right)+P_{24}U+P_{25}\Psi=0, \qquad (18)$$
$$P_{31}W^3+W^2\left(P_{32}+P_{33}L_D\right)+\Big[P_{34}\left(L_D\right)^2$$
$$+P_{35}L_D+P_{36}U+P_{37}\Psi+P_{38}\Phi_1+P_{39}$$
$$+\left(P_{310}U+P_{311}\Psi+P_{312}\Phi_1\right)\frac{L_D}{W}\Big]W \qquad (19)$$
$$+P_{313}U+P_{314}\Psi+P_{315}\Phi_1+P_{316}q=0,$$

where the parameters P_{ij} are recognized in the Appendix.

From Eqs. (17) and (18), the expressions of U and Ψ can be obtained; next, putting them into Eq. (19), leads to

$$H_1W^3+W^2\left(H_2+H_3L_D\right)+H_5W\left(L_D\right)^2$$
$$+W\left(H_4+H_6L_D+H_7\Phi_1\right) \qquad (20)$$
$$+H_8\Phi_1L_D+H_9\Phi_1+H_{10}q=0,$$

where the parameters H_n are recognized in the Appendix.

From Eq. (20), the external pressure-deflection postbuckling and thermal load-deflection postbuckling expressions are respectively obtained, as

$$q=-\frac{1}{H_{10}}\Big\{H_1W^3+W^2\left(H_3L_D+H_2\right)$$
$$+W\left[H_5\left(L_D\right)^2+H_7\Phi_1+H_4\right] \qquad (21)$$
$$\left.+H_8\Phi_1L_D+H_6WL_D+H_9\Phi_1\right\},$$

$$\Delta T=\frac{-1}{\left(WH_7+L_DH_8+H_9\right)\Gamma_1}\Big[H_{10}q+H_1W^3+W^2 \qquad (22)$$
$$\times\left(H_3L_D+H_2\right)+H_5W\left(L_D\right)^2+W\left(H_6L_D+H_4\right)\Big].$$

Eqs. (21) and (22) are employed to analyze the postbuckling behavior. Moreover, the corresponding formulations for circular plates can be readily derived by setting the curvature radius to infinity. Based on the bifurcation criterion, the thermal critical buckling loads for perfect circular plates are determined as follows

$$\Delta T_{cr}=-\frac{1}{\Gamma_1}\frac{H_4}{H_7}. \qquad (23)$$

5. Numerical investigations and discussions

Table 1 presents a comparison of the thermal critical buckling loads obtained in this study with those reported in previous works using the adjacent equilibrium criterion [1] and isogeometric finite element analysis based on FSDT and HSDT, respectively [2]. The comparison demonstrates good agreement, thereby validating the accuracy and reliability of the present analytical formulation.

In this section, a numerical investigation is conducted to analyze the buckling and postbuckling behavior of FG-GPLRC catenary caps. The material properties of the copper matrix reinforced with graphene platelets are adopted from the work of Wang et al. [17].

Table 1. Comparisons of critical thermal buckling loads ΔT_{cr} (K) of FGM circular plates with previous works [1, 2]

h/a	Najafizadeh and Hedayati [1]	Loc et al. [2]	Present
0.05	146.815	144.9953	147.0021
0.04	94.081	93.4005	94.0667
0.03	53.029	52.8191	53.3113
0.02	23.603	23.5719	23.7101
0.01	5.906	5.9093	5.9401

Table 2. Effects of GPL mass fraction on the critical thermal buckling loads $\Delta T_{cr}(K)$ of FG-GPLRC circular plates (without stiffener, $h = 0.03m$, $R = \infty$, $L_D = 0$, $m = 1$)

a/h	$T_{GPL}(\%)$	GPLRC-A	GPLRC-V	GPLRC-U	GPLRC-X	GPLRC-O
30	0	59.5779	59.5779	59.5779	59.5779	59.5779
	3	65.0846	65.0846	71.4833	89.6830	54.609
	6	72.4265	72.4265	82.4730	104.9935	61.1071
	9	79.9179	79.9179	92.6349	116.5781	68.3525
35	0	43.8404	43.8404	43.8404	43.8404	43.8404
	3	47.8814	47.8814	52.5972	66.0112	40.1662
	6	53.2777	53.2777	60.6806	77.2777	44.9423
	9	58.7860	58.7860	68.1552	85.8001	50.2700
40	0	33.5996	33.5996	33.5996	33.5996	33.5996
	3	36.6911	36.6911	40.3090	50.6005	30.7747
	6	40.8238	40.8238	46.5025	59.2353	34.4325
	9	45.0434	45.0434	52.2296	65.7659	38.5138

Table 2 investigates the effects of GPL mass fraction and distribution patterns on the thermal critical buckling loads ΔT_{cr} of FG-GPLRC circular plates, considering three radius-to-thickness ratios: a/h = 30, 35, and 40. The results clearly demonstrate that increasing the GPL mass fraction enhances the thermal buckling resistance across all distribution types. This improvement is attributed to the superior mechanical and thermal properties of GPLs, which significantly increase the effective stiffness of the composite. Notably, the X-distribution yields the highest buckling loads among all cases, followed by the U-distributions, whereas the A-, V- and O-distributions exhibit relatively modest improvements. The superior performance of the X-pattern is primarily due to its ability to concentrate GPLs near the surfaces, where the bending moment and strain energy are most pronounced, thereby maximizing structural efficiency. Furthermore, a consistent reduction in ΔT_{cr} is observed with increasing a/h ratios, indicating that thinner plates are more prone to thermal instability. This geometric sensitivity is expected, as slender structures typically exhibit lower stiffness and are thus more susceptible to thermal-induced deformation.

Fig. 2 illustrates the thermo-mechanical postbuckling responses of FG-GPLRC catenary

caps under various buckling mode assumptions. The curves indicate that higher buckling modes lead to postbuckling paths with increased stiffness and higher load-carrying capacities. In other words, the structure becomes more resistant to instability as the buckling mode number increases, and the corresponding postbuckling equilibrium paths shift upward. This behavior can be attributed to the fact that higher modes involve more complex deformation shapes that require greater strain energy to develop, making them energetically less favorable and therefore less likely to occur in practice. Consequently, although these higher-mode responses represent stiffer configurations, they are typically not critical for initial buckling under uniform loading conditions. The first buckling mode remains the most relevant from a design standpoint, as it corresponds to the lowest critical load and is most easily excited under service conditions. These results reaffirm the importance of identifying and focusing on the lowest buckling mode when evaluating the stability of shell-type structures such as FG-GPLRC catenary caps.

The comparisons of the mechanical and thermal postbuckling curves of FG-GPLRC catenary caps and spherical caps are presented in Fig. 3. Fig. 3a compares the mechanical postbuckling behavior of FG-GPLRC catenary and spherical caps under external pressure. In the initial postbuckling stage (small deflections), the catenary cap shows a lower response curve, implying reduced stiffness and lower load-bearing capacity at early deformation stages. However, as deflection increases, the postbuckling path of the catenary cap gradually surpasses that of the spherical cap, indicating greater stiffness and enhanced capacity in the large-deflection regime. This transition suggests that while catenary caps may be more compliant initially, their geometric configuration becomes increasingly favorable under large deformations, providing better structural resistance in advanced postbuckling stages. Fig. 3b illustrates the thermal postbuckling responses of FG-GPLRC catenary caps and spherical caps. Contrary to the mechanical case, the catenary cap demonstrates a lower thermal postbuckling path than the spherical cap throughout the deformation range, indicating weaker thermal buckling resistance. This suggests that under uniform thermal loading, the catenary curvature, despite its geometric advantages in mechanical contexts, may induce less favorable thermal stress redistribution, making it more vulnerable to thermally driven instability. This highlights a potential limitation of catenary caps in high-temperature environments where thermal loads dominate.

Fig. 4 investigates the mechanical and thermal postbuckling curves of the Catenary caps and circular plates with different GPL distributions.

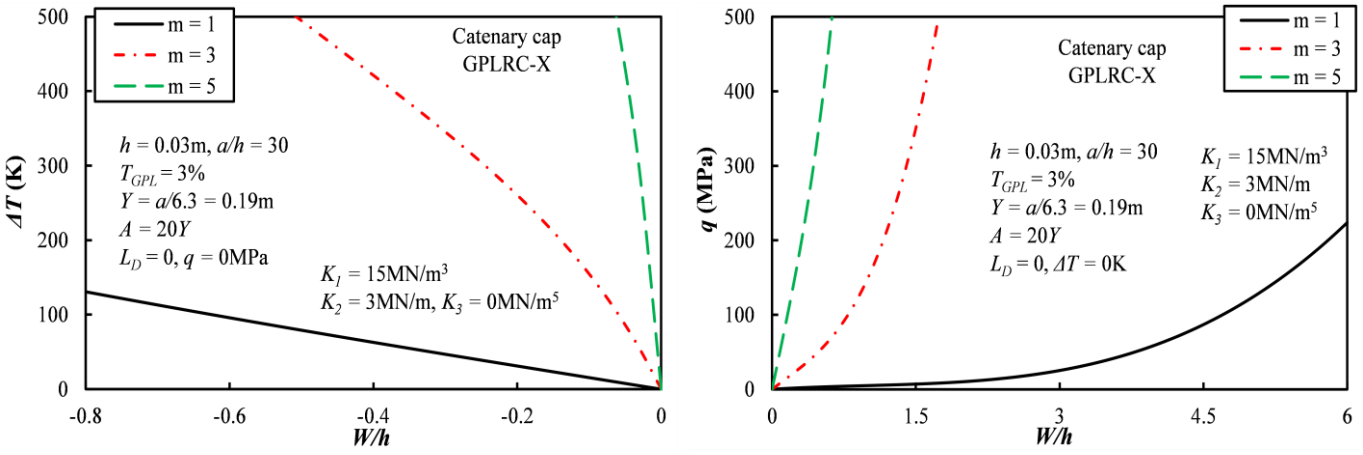

(a) (b)

Fig. 2. Thermo-mechanical postbuckling behavior of the catenary cap with different buckling modes

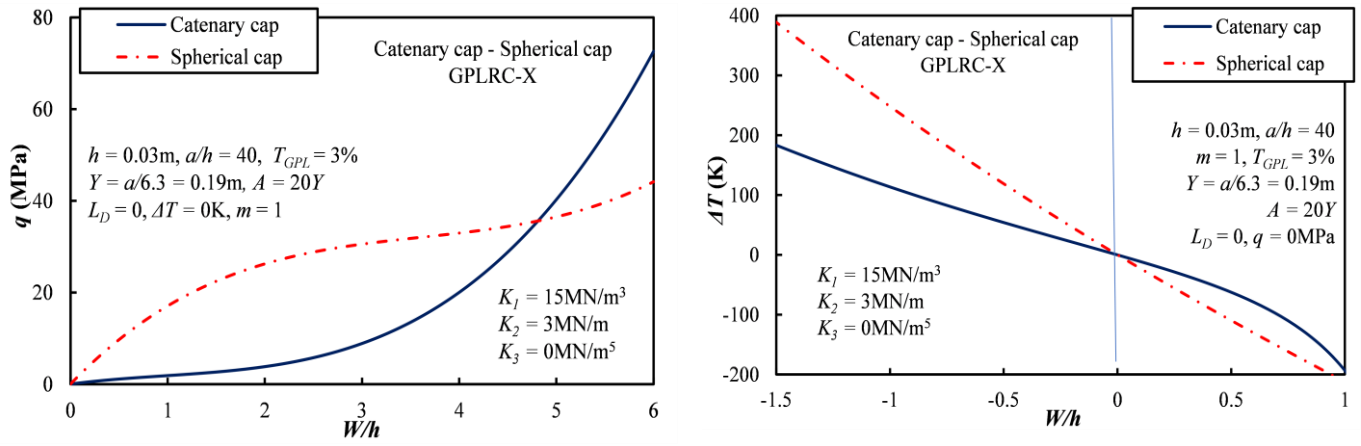

(a) (b)

Fig. 3. Comparisons of the mechanical and thermal postbuckling curves of FG-GPLRC catenary caps and spherical caps

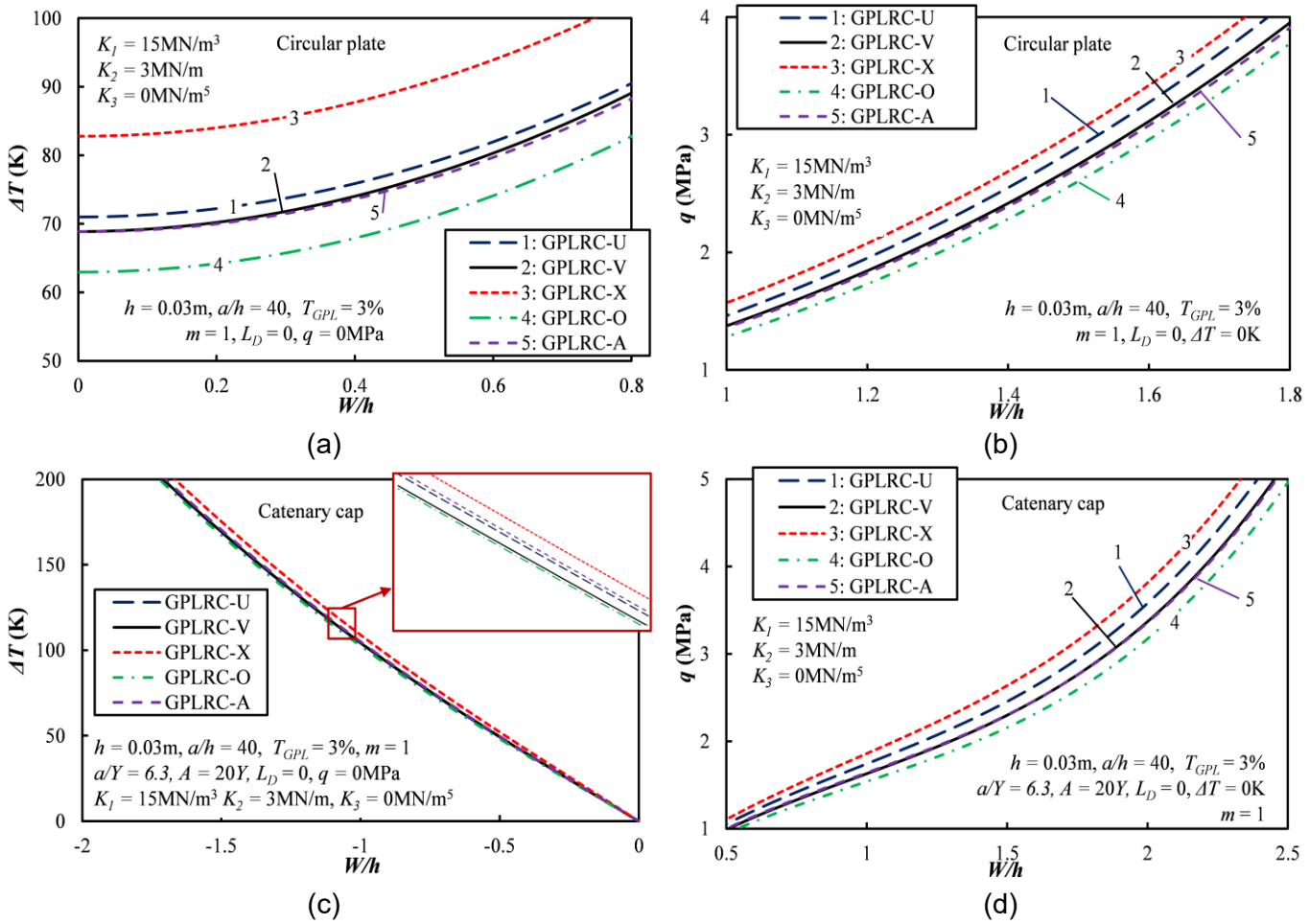

(a) (b)

(c) (d)

Fig. 4. Mechanical and thermal postbuckling curves of the catenary caps and circular plates with different GPL distributions

Figs. 4a and 4b display the mechanical and thermal postbuckling responses of FG-GPLRC circular plates with five different graphene platelet (GPL) distribution types. In both loading scenarios, the X-distribution consistently produces the highest postbuckling curves, confirming its superior reinforcement efficiency by concentrating GPLs near the surfaces, where bending moments are maximized. Following the X-type, the U-distribution shows the next highest stiffness, while the A- and

V-distributions exhibit nearly identical and moderate improvements. The O-distribution, which represents uniform reinforcement, results in the lowest postbuckling strength, highlighting its less effective stress-adaptive behavior.

Figs. 4c and 4d present the mechanical and thermal postbuckling behaviors of FG-GPLRC catenary caps, using the same GPL distribution types as in the circular plate case. The trends are consistent: the X-distribution again achieves the highest postbuckling paths, followed by U, then the closely aligned A and V distributions, and finally the O-distribution with the weakest response. However, in contrast to circular plates, the catenary caps display significantly higher postbuckling stiffness across all distribution types, especially under large deflections. This confirms the geometric advantage of the catenary shape in enhancing structural stability.

Moreover, the thermal postbuckling curves (Fig. 4d) reveal more pronounced differences among the distribution types, suggesting that GPL gradation plays a more critical role under thermal effects in curved shells.

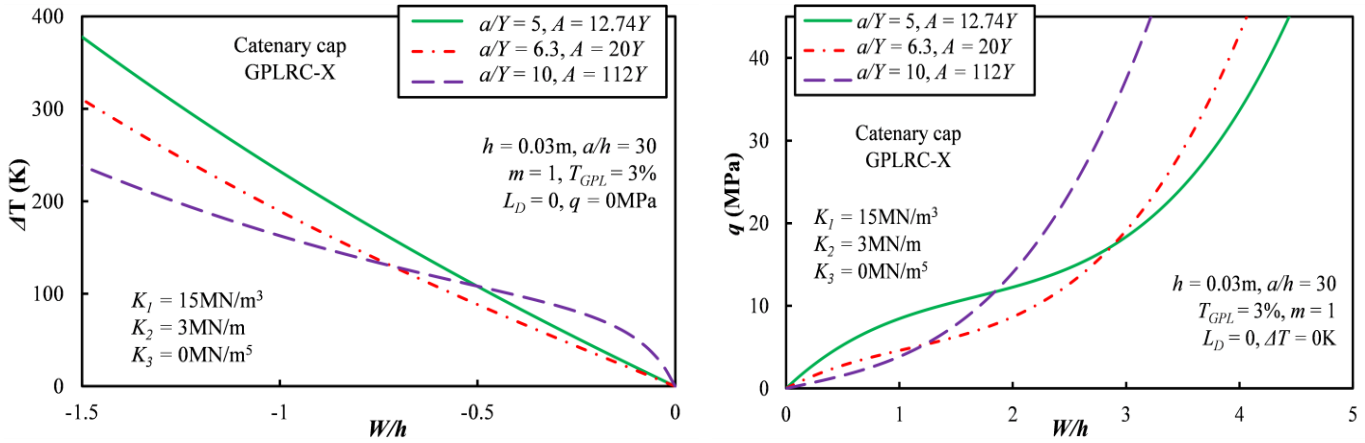

(a) (b)

Fig. 5. Mechanical and thermal postbuckling curves of the FG-GPLRC catenary cap with different a/Y ratios

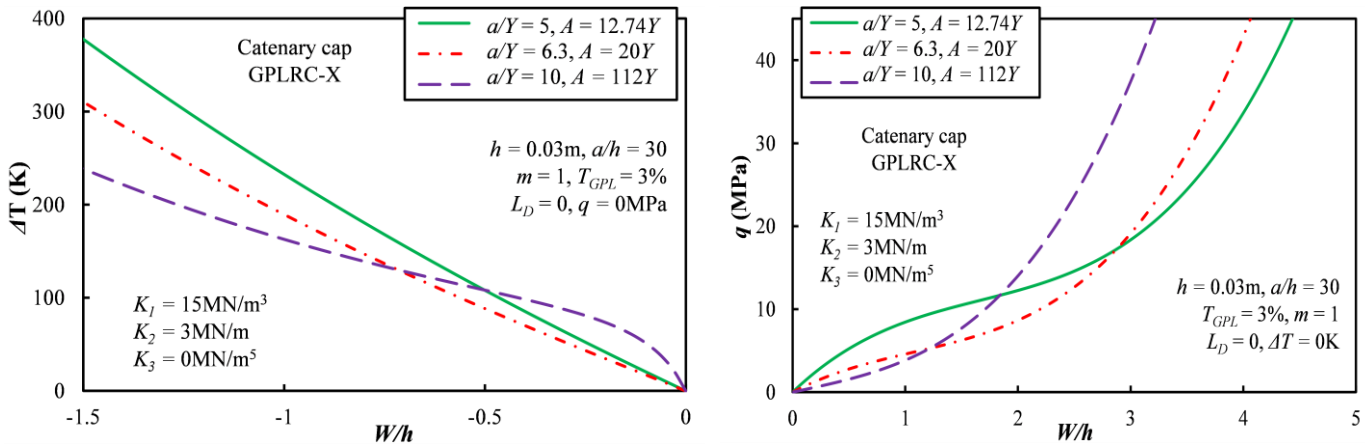

(a) (b)

Fig. 6. Mechanical and thermal postbuckling curves of the FG-GPLRC catenary with different GPL mass fractions

Fig. 5 investigates the mechanical and thermal postbuckling curves of the FG-GPLRC catenary cap with different a/Y ratios. Fig. 5a presents the thermal postbuckling responses of FG-GPLRC catenary caps with different a/Y ratios, where a is the base radius and Y is the rise of the cap. It is observed that the curvature of the cap has a significant influence on the shape and slope of

the postbuckling curves. As the cap becomes more curved (i.e., lower a/Y), the thermal postbuckling path becomes more uniform and stiffer, indicating greater resistance to thermal instability. In contrast, for shallower caps (higher a/Y), the slope of the postbuckling curve varies significantly with deflection, resembling the behavior of flat plates with initial imperfections. This behavior is consistent with the known mechanical characteristic that spherical or curved shells do not exhibit bifurcation under uniform thermal loading, unlike plates, which show clear bifurcation points. Therefore, although very shallow catenary caps may approach the behavior of plates, they still do not truly bifurcate; instead, their response mimics that of imperfect plates with gradually developing instability. Fig. 5b shows the mechanical postbuckling behavior of the same caps under external pressure. In contrast to the thermal case, the mechanical response exhibits an opposite trend in the large-deflection regime. Specifically, as the cap becomes shallower (higher a/Y), the structure demonstrates better load-carrying capacity at large deflections. Meanwhile, highly curved caps (low a/Y) exhibit greater initial stiffness but tend to localize deformation more rapidly, which may reduce their effectiveness under large mechanical deformations.

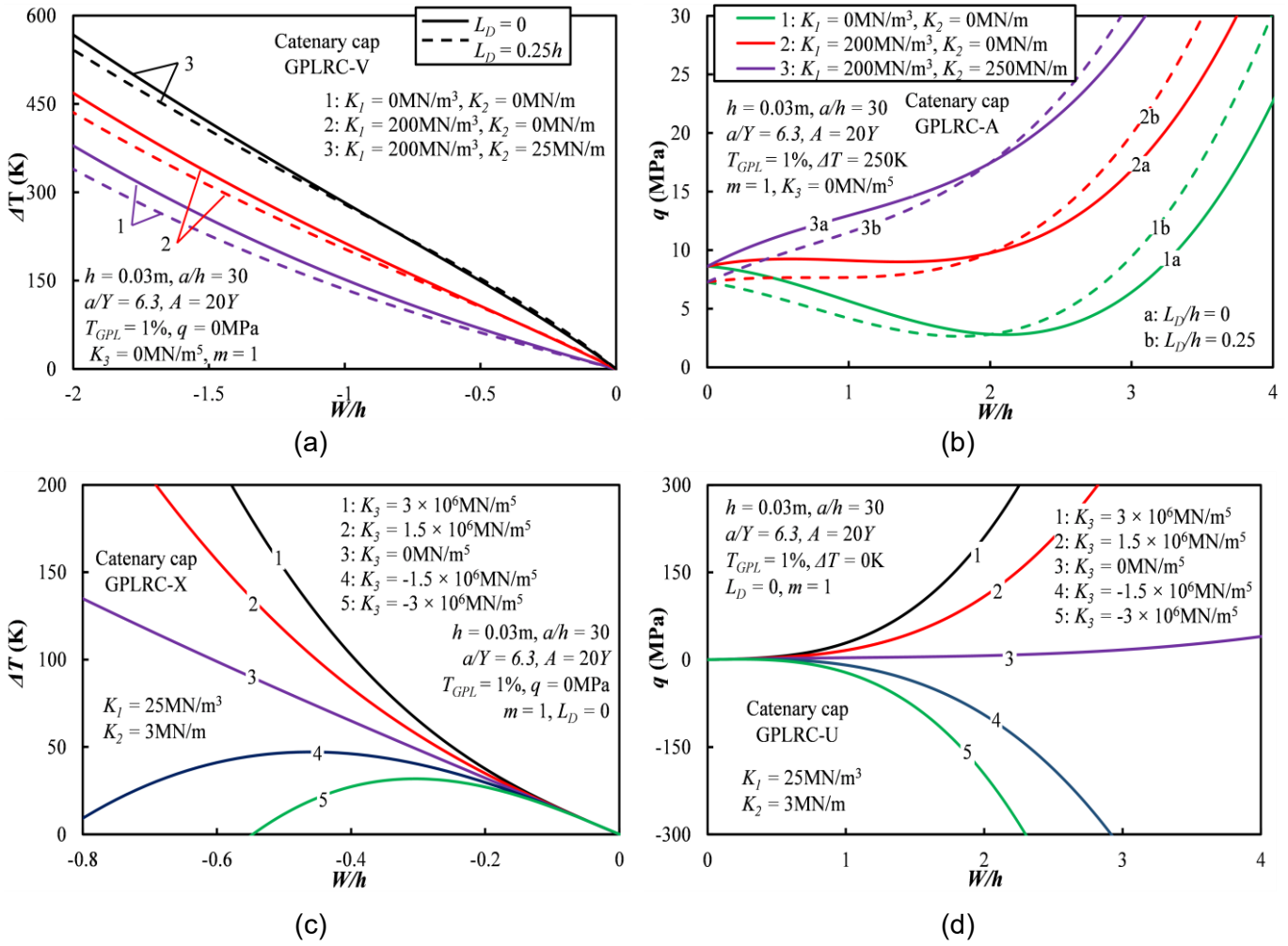

Fig. 7. Mechanical and thermal postbuckling curves of the FG-GPLRC catenary with different foundation parameters

Fig. 6 illustrates the effect of GPL mass fraction on the postbuckling behavior of FG-GPLRC catenary caps under mechanical (Fig. 6a) and thermal (Fig. 6b) loading. In both cases, an increase in GPL mass fraction leads to a clear enhancement in postbuckling stiffness and load-

carrying capacity. This is attributed to the exceptional mechanical and thermal properties of graphene platelets, which, when incorporated in higher quantities, significantly improve the composite's effective stiffness and resistance to instability. Under mechanical loading (Fig. 6a), the improvement is progressive and particularly notable at large deflections, where the enhanced reinforcement allows the structure to sustain higher loads without loss of stability.

Fig. 7 investigates the influence of elastic foundation parameters on the postbuckling responses of FG-GPLRC catenary caps under thermal and mechanical loading conditions. The foundation is modeled using a nonlinear elastic foundation characterized by three parameters: Winkler stiffness K_1, Pasternak shear coefficient K_2, and nonlinear stiffness parameter K_3.

In Figs. 7a and 7b, the combined effect of varying K_1 and K_2 is evaluated under thermal and mechanical loading, respectively. The results clearly show that increasing either or both parameters leads to a substantial enhancement in postbuckling stiffness. Under thermal loading (Fig. 7a), higher foundation stiffness restricts vertical thermal expansion, resulting in steeper and more stable postbuckling paths. Similarly, in the mechanical case (Fig. 7b), the interaction between the Winkler and Pasternak components provides both vertical and shear resistance, enabling the structure to sustain greater loads with reduced deformation. Figs. 7c and 7d focus on the effect of the nonlinear foundation parameter K_3 under thermal and mechanical loading, respectively. The nonlinear stiffness becomes increasingly influential at large deflections. In the thermal case (Fig. 7c), higher values of K_3 contribute to a more progressive and controlled postbuckling response, offsetting the destabilizing thermal stresses. In the mechanical case (Fig. 7d), the presence of nonlinear foundation stiffness helps resist excessive deformation after buckling, resulting in significantly stiffer postbuckling curves as K_3 increases.

6. Conclusion

An analytical framework was developed to study the nonlinear thermo-mechanical buckling and postbuckling behavior of FG-GPLRC catenary caps resting on nonlinear elastic foundations. The model was formulated using FSDT and von Kármán-type geometric nonlinearity, with solutions obtained via the Galerkin method. Based on the extensive numerical investigation, the following key conclusions can be drawn:

1) Among the five GPL gradation patterns, the X-distribution consistently provides the highest critical buckling loads and postbuckling stiffness due to the efficient reinforcement near the surfaces. The U-distribution follows, while A, V, and O types show lower enhancements.

2) Increasing the GPL content significantly improves the structural stiffness and load-bearing capacity under both thermal and mechanical loading conditions. The improvement is particularly notable at large deflections.

3) The curvature of the catenary cap plays a crucial role. In thermal loading, more curved caps (lower a/Y) offer more stable and stiffer postbuckling responses. In contrast, under mechanical loading, shallower caps (higher a/Y) provide better capacity at large deformations, while more curved ones exhibit higher initial stiffness.

4) Catenary caps outperform circular plates and spherical caps in mechanical postbuckling performance, especially under large deflections. However, they may show reduced thermal resistance compared to spherical caps under uniform heating.

5) Increasing Winkler and Pasternak stiffness improves both thermal and mechanical postbuckling behavior by providing stronger vertical and shear support. The nonlinear foundation parameter K_3 becomes dominant at large deflections, enhancing structural stability

significantly under both types of loading.

References

[1] M.M. Najafizadeh, B. Hedayati. (2004). Refined theory for thermoelastic stability of functionally graded circular plates. *Journal of Thermal Stresses*, 27 (9), 857-880. https://doi.org/10.1080/01495730490486532

[2] V.T. Loc, H.T. Chien, N.X. Hung. (2013). An isogeometric finite element formulation for thermal buckling analysis of functionally graded plates. *Finite Elements in Analysis and Design*, 73, 65-76. https://doi.org/10.1016/j.finel.2013.05.003

[3] Y. Kiani. (2017). Axisymmetric static and dynamics snap-through phenomena in a thermally postbuckled temperature-dependent FGM circular plate. *International Journal of Non-Linear Mechanics*, 89, 1–13. https://doi.org/10.1016/j.ijnonlinmec.2016.11.003

[4] R. Ansari, M. Zargar Ershadi, M. Faraji Oskouie, H. Rouhi. (2023). A VDQ approach to nonlinear vibration analysis of functionally graded porous circular plates resting on elastic foundation under hygrothermal shock. *Acta Mechanica*, 234, 5115–5129. https://doi.org/10.1007/s00707-023-03649-5

[5] R. Lal, R. Saini. (2020). Vibration analysis of FGM circular plates under non-linear temperature variation using generalized differential quadrature rule. *Applied Acoustics*, 158, 107027. https://doi.org/10.1016/j.apacoust.2019.107027

[6] C. Gao, F. Pang, H. Li, D. Jia, Y. Tang. (2022). Steady and transient vibration analysis of uniform and stepped annular/circular plates based on FSDT. *Acta Mechanica,* 233, 1061–1082. https://doi.org/10.1007/s00707-022-03157-y

[7] R. Shahsiah, M.R. Eslami, R. Naj. (2006). Thermal instability of functionally graded shallow spherical shell. *Journal of Thermal Stresses,* 29 (8), 771–790. https://doi.org/10.1080/01495730600705406

[8] M.S. Boroujerd, M.R. Eslami. (2013). Nonlinear axisymmetric thermomechanical response of piezo-FGM shallow spherical shells. *Archive of Applied Mechanics*, 83, 1681–1693. https://doi.org/10.1007/s00419-013-0769-y

[9] M.S. Boroujerd, M.R. Eslami. (2014). Axisymmetric snap-through behavior of Piezo-FGM shallow clamped spherical shells under thermo-electro-mechanical loading. *International Journal Of Pressure Vessels And Piping*, 120-121, 19–26. https://doi.org/10.1016/j.ijpvp.2014.03.008

[10] M. Javani, Y. Kiani, M.R. Eslami. (2024). Nonlinear dynamic response of a temperature-dependent FGM spherical shell under various boundary conditions and thermal shocks: Examination of dynamic snap-through. *Thin-Walled Structures*, 199, 111796. https://doi.org/10.1016/j.tws.2024.111796

[11] N.T. Phuong, V.H. Nam, D.T. Dong. (2020). Nonlinear vibration of functionally graded sandwich shallow spherical caps resting on elastic foundations by using first-order shear deformation theory in thermal environment. *Journal of Sandwich Structures and Materials*, 22 (4), 1157-1183. https://doi.org/10.1177/1099636218782645

[12] L.N. Ly, D.T.N. Thu, D.T. Dong, V.M. Duc, B.T. Tu, N.T. Phuong, V.H. Nam. (2023). A Novel Analytical Approach for Nonlinear Thermo-Mechanical Buckling of Higher-Order Shear Deformable Porous Circular Plates and Spherical caps with FGM Face Sheets. *International Journal of Applied Mechanics*, 15 (05), 2350035. https://doi.org/10.1142/S1758825123500357

[13] J.P. Song, G.L. She, M.A. Eltaher. (2024). Nonlinear aero-thermo-elastic flutter analysis of stiffened graphene platelets reinforced metal foams plates with initial geometric imperfection. *Aerospace Science and Technology*, 147, 109050. https://doi.org/10.1016/j.ast.2024.109050

[14] Y.P. Li, G.L. She. (2025). Nonlinear dynamic response of graphene platelets reinforced cylindrical shells under moving loads considering initial geometric imperfection. *Engineering Structures*, 323 (Part A), 119241. https://doi.org/10.1016/j.engstruct.2024.119241

[15] M. Khatoonabadi, M. Jafari, F. Kiarasi, M. Hosseini, M. Babaei, K. Asemi. (2023). Shear buckling response of FG porous annular sector plate reinforced by graphene platelet subjected to different shear loads. *Journal of Computational Applied Mechanics*, 54(1), 68-86. DOI:10.22059/JCAMECH.2023.352182.784

[16] K. Asemi, M. Babaei, F. Kiarasi. (2022). Static, natural frequency and dynamic analyses of functionally graded porous annular sector plates reinforced by graphene platelets. *Mechanics Based Design of Structures and Machines*, 50 (11), 3853–3881. https://doi.org/10.1080/15397734.2020.1822865

[17] Y. Wang, R. Zeng, M. Safarpour. (2022). Vibration analysis of FG-GPLRC annular plate in a thermal environment. *Mechanics Based Design of Structures and Machines*, 50 (1), 352–370. https://doi.org/10.1080/15397734.2020.1719508

[18] M. Javani, Y. Kiani, M.R. Eslami. (2021). Geometrically nonlinear free vibration of FG-GPLRC circular plate on the nonlinear elastic foundation. *Composite Structures*, 261, 113515. https://doi.org/10.1016/j.compstruct.2020.113515

[19] Z. Dai, H. Tang, S. Wu, M. Habibi, Z. Moradi, H.E. Ali. (2023). Nonlinear consecutive dynamic instabilities of thermally shocked composite circular plates on the softening elastic foundation. *Thin-walled structures*, 186, 110645. https://doi.org/10.1016/j.tws.2023.110645

[20] J. Wang, X. Jiang. (2024). Application of bilateral iterative displacement control method to nonlinear free vibration analysis of dual-FG nanocomposite circular plates. *Communications in Nonlinear Science and Numerical Simulation*, 138, 108236. https://doi.org/10.1016/j.cnsns.2024.108236

[21] A. Sankar, S. El-Borgi, T. Ben Zineb, M. Ganapathi. (2016). Dynamic snap-through buckling of CNT reinforced composite sandwich spherical caps. *Composites Part B: Engineering*, 99, 472-482. https://doi.org/10.1016/j.compositesb.2016.06.027

[22] D. Liu, Y. Zhou, J. Zhu. (2021). On the free vibration and bending analysis of functionally graded nanocomposite spherical shells reinforced with graphene nanoplatelets: Three-dimensional elasticity solutions. *Engineering Structures*, 226, 111376. https://doi.org/10.1016/j.engstruct.2020.111376

[23] L.N. Ly, B.T. Tu, D.T.N. Thu, D.T. Dong, V.M. Duc, N.T. Phuong. (2023). Nonlinear thermo-mechanical buckling and postbuckling of sandwich FG-GPLRC spherical caps and circular plates with porous core by using higher-order shear deformation theory. *Journal of Thermoplastic Composite Materials*, 36 (10), 4083-4105. https://doi.org/10.1177/08927057221147827

[24] N.T. Phuong, D.T. Dong, B.T. Tu, V.M. Duc, L.N. Khuong, P.T. Hieu, V.H. Nam. (2024). Nonlinear thermo-mechanical axisymmetric stability of FG-GPLRC spherical shells and circular plates resting on nonlinear elastic medium. *Ships and Offshore Structures*, 19 (6), 820-830. https://doi.org/10.1080/17445302.2023.2214489

[25] Z. Zhou, Y. Wang, S. Zhang, R. Dimitri, F. Tornabene, K. Asemi. (2023). Numerical Study on the Buckling Behavior of FG Porous Spherical Caps Reinforced by Graphene

Platelets. *Nanomaterials*, 13 (7), 1205. doi: 10.3390/nano13071205

[26] X. Shen, T. Li, L. Xu, F. Kiarasi, M. Babaei, K. Asemi. (2024). Free vibration analysis of FG porous spherical cap reinforced by graphene platelet resting on Winkler foundation. *Advanced Nano Research*, 16 (1), 11-26. https://doi.org/10.12989/anr.2024.16.1.011

[27] D. Chen, M. Mou, A. Hozuri. (2023). Dynamic and electrical damping of deep spherical sandwich shells with electrorheological fluid core and FG-GPLRC skins. *European Journal of Mechanics - A/Solids*, 98, 104898. https://doi.org/10.1016/j.euromechsol.2022.104898

[28] Y. Heydarpour, P. Malekzadeh, F. Gholipour. (2019). Thermoelastic analysis of FG-GPLRC spherical shells under thermo-mechanical loadings based on Lord-Shulman theory. *Composites Part B: Engineering*, 164, 400-424. https://doi.org/10.1016/j.compositesb.2018.12.073

[29] V.H. Nam, T.Q. Minh, P.T. Hieu, V.T. Hung, B.T. Tu, N.T.T. Hoai, D.T. Dong. (2023). A new analytical approach for nonlinear thermo-mechanical postbuckling of FG-GPLRC circular plates and shallow spherical caps stiffened by spiderweb stiffeners. *Thin-Walled Structures*, 193, 111296. https://doi.org/10.1016/j.tws.2023.111296

[30] V.H. Nam, C.V. Doan, N.T. Phuong. (2023). A new analytical approach to the nonlinear buckling and postbuckling behavior of functionally graded graphene reinforced composite laminated cylindrical, parabolic, and half-sinusoid shallow imperfect panels. *Polymer Composites*, 44 (12), 8928-8945. https://doi.org/10.1002/pc.27748

[31] T.Q. Minh, V.H. Nam, V.M. Duc, V.T. Hung, L.N. Ly, N.T. Phuong. (2024). Nonlinear vibration and dynamic buckling responses of stiffened functionally graded graphene-reinforced cylindrical, parabolic, and sinusoid panels using the higher-order shear deformation theory. *ZAMM - Journal of Applied Mathematics and Mechanics / Zeitschrift für Angewandte Mathematik und Mechanik,* 104 (3), e2023005802024. https://doi.org/10.1002/zamm.202300580

[32] N.T. Phuong, V.M. Duc, N.T. Giang, L.N. Ly, N.T.T. Xuan, V.H. Nam. (2024). Nonlinear vibration and dynamic buckling of complex curved functionally graded graphene panels reinforced with inclined stiffeners. *International Journal of Structural Stability and Dynamics*, 24 (19), 2450223. https://doi.org/10.1142/S0219455424502237

[33] V.H. Nam, B.T. Tu, V.T. Hung, C.V. Doan, N.T. Phuong. (2025). Nonlinear thermomechanical buckling and postbuckling analysis of sandwich FG-GPLRC complexly curved caps and circular plates with porous core. *Acta Mechanica*, 236, 421–438. https://doi.org/10.1007/s00707-024-04152-1

[34] B.T. Tu, N.T. Phuong, L.N. Ly, V.T. Hung, V.H. Nam. (2025). A New Analytical Approach to the Nonlinear Thermo-Mechanical Buckling Behavior of Three-Dimensional Graphene Foams-Reinforced Complexly Curved Caps and Circular Plates. *International Journal of Structural Stability and Dynamics*, 25(16), 2550169. https://doi.org/10.1142/S021945542550169X

[35] B.T. Tu, L.N. Ly, N.T. Phuong. (2022). A new analytical approach of nonlinear thermal buckling of FG-GPLRC circular plates and shallow spherical caps using the FSDT and Galerkin method. *Vietnam Journal of Mechanics*, 44 (4), 418–430. https://doi.org/10.15625/0866-7136/17932

APPENDIX

$$P_{11} = -\frac{1}{36}\frac{\pi m\left[1+(-1)^m\right]}{a}\left(-3A_{12}+A_{11}\right),$$

$$P_{12} = \int_0^a \left\{\frac{\pi mr}{2aR}\left[\sin\left(\frac{\pi mr}{a}\right)\right]^2 + \left[\cos\left(\frac{\pi mr}{2a}\right)\frac{r}{R^2}\sin\left(\frac{\pi mr}{a}\right)\right]^2\frac{dR}{dr}\right\}\left(A_{11}+A_{12}\right) + \\ + \frac{1}{R}\sin\left(\frac{\pi mr}{a}\right)\left(A_{22}-A_{11}\right)\left[\cos\left(\frac{\pi mr}{2a}\right)\right]^2 dr,$$

$$P_{13} = -\frac{1}{18}\left\{A_{11}\left[(-1)^m-1\right]+3\left[(-1)^{1+m}+1\right]A_{12}\right\}\frac{\pi m}{a},$$

$$P_{14} = -\int_0^a \frac{A_{22}}{r}\left[\sin\left(\frac{\pi mr}{a}\right)\right]^2 dr - \frac{\pi^2m^2}{4}A_{11}, \quad P_{15} = -\int_0^a \frac{B_{22}}{r}\left[\sin\left(\frac{\pi mr}{a}\right)\right]^2 dr - \frac{\pi^2m^2}{4}B_{11},$$

$$P_{21} = \left[1-(-1)^m\right]\frac{\pi m}{36a}\left(B_{11}-3B_{12}\right),$$

$$P_{22} = \int_0^a \left\{\left[\frac{\pi mr}{2aR}\left(\sin\left(\frac{\pi mr}{a}\right)\right)^2 + \sin\left(\frac{\pi mr}{a}\right)\frac{r}{R^2}\frac{d}{dr}R\left(\cos\left(\frac{\pi mr}{2a}\right)\right)^2\right]\left(B_{11}+B_{12}\right)\right. \\ \left. + \frac{m\pi a}{8}K_S H_{44} + \sin\left(\frac{\pi mr}{a}\right)\frac{1}{R}\left(B_{22}-B_{11}\right)\left(\cos\left(\frac{\pi mr}{2a}\right)\right)^2\right\} dr,$$

$$P_{23} = -\frac{1}{18}\left[B_{11}\left[(-1)^m-1\right]+\left[(-1)^{1+m}+1\right]3B_{12}\right]\frac{\pi m}{a},$$

$$P_{24} = -\int_0^a \left[\frac{B_{22}}{r}\left(\sin\left(\frac{\pi mr}{a}\right)\right)^2\right]dr - \frac{\pi^2m^2}{4}B_{11},$$

$$P_{25} = -\int_0^a \left[\frac{D_{22}}{r}\left(\sin\left(\frac{\pi mr}{a}\right)\right)^2\right]dr + \frac{1}{4}\left(-a^2K_S H_{44} - \pi^2m^2D_{11}\right),$$

$$P_{31} = -\frac{\pi^2m^2}{512a^2}\left[16\left(\cos\left(\frac{\pi m}{2}\right)\right)^8 + 4\left(\cos\left(\frac{\pi m}{2}\right)\right)^4 - 32\left(\cos\left(\frac{\pi m}{2}\right)\right)^6 + \right. \\ \left. + 3\pi^2m^2 + 12\left(\cos\left(\frac{\pi m}{2}\right)\right)^2\right]A_{11} - \frac{a^2}{2304\pi^2m^2}\left[144\left(\cos\left(\frac{\pi m}{2}\right)\right)^8\right. \\ \left. + 420\left(\cos\left(\frac{\pi m}{2}\right)\right)^4 + 224\left(\cos\left(\frac{\pi m}{2}\right)\right)^6 + 315\pi^2m^2 + 1260\left(\cos\left(\frac{\pi m}{2}\right)\right)^2 - 2048\right]K_3,$$

$$P_{32} = -\int_0^a \frac{\pi m}{a^2R^2}\left(\cos\left(\frac{\pi mr}{2a}\right)\right)^4\left(A_{11}+A_{12}\right)\left[-\frac{3\pi}{2}\left(\cos\left(\frac{\pi mr}{2a}\right)\right)^2 Rmr + \right. \\ \left. + \left(r\frac{dR}{dr}-R\right)\frac{a}{2}\sin\left(\frac{\pi mr}{a}\right) + \pi mrR\right]dr,$$

$$P_{33} = -\frac{3\,\pi^2\,m^2}{512\,a^2}A_{11}\left[16\left(\cos\left(\frac{\pi m}{2}\right)\right)^8 + 4\left(\cos\left(\frac{\pi m}{2}\right)\right)^4 - 32\left(\cos\left(\frac{\pi m}{2}\right)\right)^6 + 12\left(\cos\left(\frac{\pi m}{2}\right)\right)^2 + 3\,\pi^2 m^2\right],$$

$$P_{34} = \frac{m^2\pi^2}{256\,a^2}(-A_{11})\left[16\left(\cos\left(\frac{\pi m}{2}\right)\right)^8 + 12\left(\cos\left(\frac{\pi m}{2}\right)\right)^2 - 32\left(\cos\left(\frac{\pi m}{2}\right)\right)^6 + 4\left(\cos\left(\frac{\pi m}{2}\right)\right)^4 + 3\,\pi^2 m^2\right],$$

$$P_{35} = -\int_0^a \frac{\pi m}{a^2 R^2}\left(\cos\left(\frac{\pi m r}{2a}\right)\right)^4 (A_{11} + A_{12})\left[-\pi m r R\left(\cos\left(\frac{\pi m r}{2a}\right)\right)^2 + \frac{\pi m r R}{2} + \frac{a}{2}\sin\left(\frac{\pi m r}{a}\right)\left(r\frac{dR}{dr} - R\right)\right]dr,$$

$$P_{36} = \frac{\pi m}{9a}A_{11}\left[2\left(\cos\left(\frac{\pi m}{2}\right)\right)^6 + 1 - 3\left(\cos\left(\frac{\pi m}{2}\right)\right)^4\right] + \frac{\pi m}{3a}A_{12}\left[4\left(\cos\left(\frac{\pi m}{2}\right)\right)^6 - 1 - 3\left(\cos\left(\frac{\pi m}{2}\right)\right)^4\right],$$

$$P_{37} = B_{11}\left[2\left(\cos\left(\frac{\pi m}{2}\right)\right)^6 + 1 - 3\left(\cos\left(\frac{\pi m}{2}\right)\right)^4\right]\frac{\pi m}{9a} + + B_{12}\left[4\left(\cos\left(\frac{\pi m}{2}\right)\right)^6 - 1 - 3\left(\cos\left(\frac{\pi m}{2}\right)\right)^4\right]\frac{\pi m}{3a},$$

$$P_{38} = -\frac{1}{16}\left\{4\left[\left(\cos\left(\frac{\pi m}{2}\right)\right)^4 - \left(\cos\left(\frac{\pi m}{2}\right)\right)^2\right] - \pi^2 m^2\right\},$$

$$P_{39} = \left(\cos\left(\frac{\pi m}{2}\right)\right)^4 \frac{m^2\pi^2\left(K_2 + K_s H_{44}\right) - a^2 K_1}{4\pi^2 m^2} - \left(\cos\left(\frac{\pi m}{2}\right)\right)^2 \frac{m^2\pi^2\left(K_2 + K_s H_{44}\right) + 3a^2 K_1}{4\pi^2 m^2} - \int_0^a \frac{r\left(2A_{12} + A_{11} + A_{22}\right)}{R^2}\left(\cos\left(\frac{\pi m r}{2a}\right)\right)^4 dr - \frac{m^4\pi^4\left(K_2 + K_s H_{44}\right) + a^2 K_1\left(3\pi^2 m^2 - 16\right)}{16\pi^2 m^2},$$

$$P_{310} = \frac{\pi m}{9a}\left[2\left(\cos\left(\frac{\pi m}{2}\right)\right)^6 + 1 - 3\left(\cos\left(\frac{\pi m}{2}\right)\right)^4\right]A_{11} + \frac{\pi m}{3a}\left[4\left(\cos\left(\frac{\pi m}{2}\right)\right)^6 - 1 - \left(\cos\left(\frac{\pi m}{2}\right)\right)^4\right]A_{12},$$

$$P_{311}=\frac{\pi m}{9a}\left[2\left(\cos\left(\frac{\pi m}{2}\right)\right)^6+1-3\left(\cos\left(\frac{\pi m}{2}\right)\right)^4\right]B_{11}$$
$$+\frac{\pi m}{3a}\left[4\left(\cos\left(\frac{\pi m}{2}\right)\right)^6-1-3\left(\cos\left(\frac{\pi m}{2}\right)\right)^4\right]B_{12},$$

$$P_{312}=\frac{1}{16}\left\{\pi^2m^2+4\left[\left(\left(\cos\left(\frac{\pi m}{2}\right)\right)^2-\cos\left(\frac{\pi m}{2}\right)\right)^4\right]\right\},$$

$$P_{313}=\int_0^a\left[\frac{1}{R}(A_{12}+A_{22})\sin\left(\frac{\pi mr}{a}\right)+\frac{r\pi m}{aR}(A_{11}+A_{12})\left(\cos\left(\frac{\pi mr}{2a}\right)\right)^2\cos\left(\frac{\pi mr}{a}\right)\right]dr,$$

$$\kappa_{314}=\frac{m\pi a}{8}K_sH_{44}+$$
$$+\left(\cos\left(\frac{\pi mr}{2a}\right)\right)^2\int_0^a\left[\frac{1}{R}(B_{12}+B_{22})\sin\left(\frac{\pi mr}{a}\right)+\frac{\pi mr}{aR}(B_{11}+B_{12})\cos\left(\frac{\pi mr}{a}\right)\right]dr,$$

$$P_{315}=-\int_0^a\left(\cos\left(\frac{\pi mr}{2a}\right)\right)^2\frac{2r}{R}dr\,,\qquad P_{316}=\left\{\pi^2m^2-1+4\left[\left(\cos\left(\frac{\pi m}{2}\right)\right)^2\right]\right\}\frac{a^2}{4\pi^2m^2}.$$

$$H_1=P_{31}-\frac{(P_{11}P_{25}-P_{15}P_{21})P_{36}}{P_{14}P_{25}-P_{15}P_{24}}+\frac{(P_{11}P_{24}-P_{14}P_{21})P_{37}}{P_{14}P_{25}-P_{15}P_{24}},$$

$$H_2=P_{32}+\frac{(P_{12}P_{24}-P_{14}P_{22})P_{37}}{P_{14}P_{25}-P_{15}P_{24}}+\frac{P_{314}(P_{11}P_{24}-P_{14}P_{21})}{P_{14}P_{25}-P_{15}P_{24}}$$
$$-\frac{(P_{12}P_{25}-P_{15}P_{22})P_{36}}{P_{14}P_{25}-P_{15}P_{24}}-\frac{P_{313}(P_{11}P_{25}-P_{15}P_{21})}{P_{14}P_{25}-P_{15}P_{24}},$$

$$H_3=P_{33}+\frac{(P_{13}P_{24}-P_{14}P_{23})P_{37}}{P_{14}P_{25}-P_{15}P_{24}}-\frac{(P_{11}P_{25}-P_{15}P_{21})P_{310}}{P_{14}P_{25}-P_{15}P_{24}}$$
$$+\frac{(P_{11}P_{24}-P_{14}P_{21})P_{311}}{P_{14}P_{25}-P_{15}P_{24}}-\frac{(P_{13}P_{25}-P_{15}P_{23})P_{36}}{P_{14}P_{25}-P_{15}P_{24}},$$

$$H_4=P_{39}+\frac{P_{314}(P_{12}P_{24}-P_{14}P_{22})}{P_{14}P_{25}-\kappa_{15}P_{24}}-\frac{P_{313}(P_{12}P_{25}-P_{15}P_{22})}{P_{14}P_{25}-P_{15}P_{24}},$$

$$H_5=\frac{(P_{13}P_{24}-P_{14}P_{23})P_{311}}{P_{14}P_{25}-P_{15}P_{24}}+P_{34}-\frac{(P_{13}P_{25}-P_{15}P_{23})P_{310}}{P_{14}P_{25}-P_{15}P_{24}},$$

$$H_6=\frac{(P_{12}P_{24}-P_{14}P_{22})P_{311}}{P_{14}P_{25}-P_{15}P_{24}}+P_{35}-\frac{(P_{12}P_{25}-P_{15}P_{22})P_{310}}{P_{14}P_{25}-P_{15}P_{24}}$$
$$+\frac{P_{313}(P_{15}P_{23}-P_{13}P_{25})}{P_{14}P_{25}-P_{15}P_{24}}-\frac{P_{314}(P_{14}P_{23}-P_{13}P_{24})}{P_{14}P_{25}-P_{15}P_{24}},$$

$$H_7=P_{38},\qquad H_8=P_{312},\qquad H_9=P_{315},\qquad H_{10}=P_{316}.$$